

# Behavior of three modes of decay channels and their self-energies of elliptic dielectric microcavity

Kyu-Won Park,<sup>1</sup> Jaewan Kim,<sup>2</sup> and Kabgyun Jeong<sup>3,2,\*</sup>

<sup>1</sup>*Department of Physics, Sogang University, Seoul 04107, Korea*

<sup>2</sup>*School of Computational Sciences, Korea Institute for Advanced Study, Seoul 02455, Korea*

<sup>3</sup>*Center for Macroscopic Quantum Control, Department of Physics and Astronomy, Seoul National University, Seoul 08826, Korea*

(Dated: December 9, 2024)

The Lamb shift (self-energy) of an elliptic dielectric microcavity is studied. We show that the size of Lamb shift, which is a small energy shift due to the system-environment coupling in quantum regime, is dependent on the geometry of boundary condition. It shows a global transition depending on the eccentricity of the ellipsis. These transitions can be classified into three types of decay channels known as whispering gallery modes, stable bouncing ball modes, and unstable bouncing ball modes. These modes are manifested through the Poincaré surface of section with Husimi distribution function on classical phase space. It is found that the similarity (measured in Bhattacharyya distance) between the Husimi distributions below critical lines of two different modes increases as the difference of their self-energies decreases when the quality factors of the modes are in the same order of magnitude.

PACS numbers: 42.60.Da, 42.50.-p, 42.50.Nn, 12.20.-m, 13.40.Hq

## I. INTRODUCTION

Understanding an open effect on a quantum system, i.e., coupling the system to their environment, is very important in a dielectric microcavity. For examples, Fresnel filtering [1, 2], Goos-Hänchen shift [3, 4], quasi-scar [5], and exceptional point [6–8] are only possible in open quantum systems. As well as most typical (real) systems are open systems interacting with their environment, and it is in contrast to the perfect closed (or so-called billiard) system [9–11], which is established by the infinite potential well.

A way to investigate the open nature of a quantum system is to look into the phenomenon known as Lamb shift. The Lamb shift is a tiny energy transition of a quantum system originated from the system-environment coupling or caused by the vacuum fluctuations [12, 13]. This Lamb shift is initially observed for a hydrogen atom [12], but these effects have been generalized to cavity QED [14], photonic crystals [15], and also a circular dielectric microcavity [16]. Especially, the non-Hermitian Hamiltonian [17–20] via Feshbach projection-operator formalism was introduced to define the Lamb shift in a dielectric microcavity—the difference of energy eigenvalues between the effective non-Hermitian Hamiltonian and the Hermitian Hamiltonian for a closed system is first defined as a Lamb shift in Ref. [16].

Recently, it is known that there are two kinds of Lamb shift [13, 21, 22]. First one is *self-energy*, that is, the Lamb shift in atomic physics, and the other is a *collective* Lamb shift. The considerable difference of these two Lamb shifts will be clear soon, when we explicitly write

down the matrix elements of an effective non-Hermitian Hamiltonian. Here, the diagonal terms are corresponding to self-energy itself and the off-diagonals are directly corresponding to the collective Lamb shift, respectively [23]. In this paper, we consider a dependence of the geometrical boundary conditions of the self-energy by global transitions, and compare between the relative difference of self-energy and similarity of decay channels by Bhattacharyya distance.

This paper is organized as follows. We introduce a Poincaré surface of section (PSOS) for boundary conditions in an elliptic billiard in Sec. II. In Sec. III, we briefly review the non-Hermitian Hamiltonian and two kinds of Lamb shift. The dependence on geometrical boundary conditions of self-energy and global transitions are presented in Sec. IV. Our main result of crossings of self-energies is discussed in Sec. V. Finally, we conclude the paper in Sec. VI.

## II. CANONICAL COORDINATE AND POINCARÉ SURFACE OF SECTION

The Poincaré surface of section (PSOS) [24] is very useful tool to analyze a ray dynamics on microcavities. For given boundary condition of a convex billiard system, we can efficiently record not only the sequences of bouncing points  $S$  along the boundary wall but also the successive values of  $\sin \chi$ , where  $\chi$  is the incident angle with respect to the normal to the boundary wall. Then we obtain pairs of sequences of points  $(S, \sin \chi)$  corresponding to PSOS (See Fig. 1 below). This plot represents a section through the classical phase space not entire phase space itself. So we can analyze the ray dynamics easily, since we deal with it under one-lower dimension.

Furthermore,  $\sin \chi$  is proportional to the tangential

---

\*Electronic address: kgjeong6@snu.ac.kr

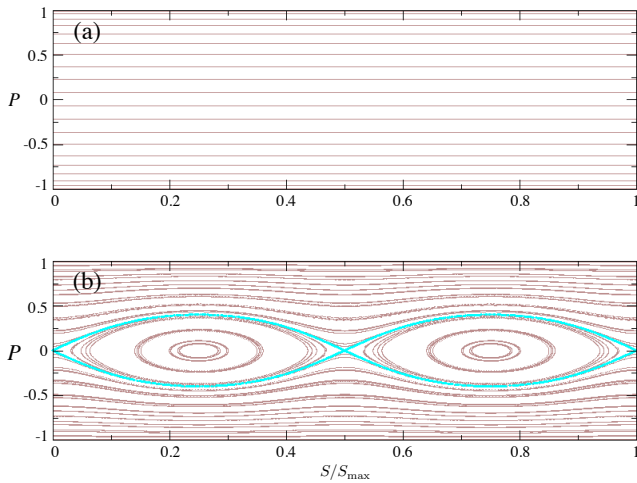


FIG. 1: Poincaré surface of section. (a) Poincaré surface of section for a circle. Because of the angular momentum conservation, the tangent momentum  $P := \sin \chi$  is straight line depending on arc-length  $S$ . (b) Poincaré surface of section for an ellipse. There are primary two types of region. One is whispering gallery motions, and another one is bouncing ball motions: These two regions are divided by the separatrix whose color is cyan. The bouncing ball motions also are classified into the stable-island motion and unstable-saddle motion.

component of the momentum at each collision with boundary, and this momentum component is canonical conjugate momentum with respect to the boundary length  $S$  [25].

We here plot the PSOS for a circle in Fig. 1(a). In the case of circle, since the incident angles and reflection angles are same to have angular momentum conservation, the tangent momentum  $P = \sin \chi$  is straight line depending on arc length  $S$ . There is a PSOS for ellipse at eccentricity  $e = 0.4$  in Fig 1(b), which are mainly two types of region. One is a corresponding to whispering gallery motion and the other is a bouncing ball motions. These two regions are divided by separatrix whose color is cyan. The bouncing ball motions also can be divided into stable-island motion and unstable-saddle motion.

### III. NON-HERMITIAN HAMILTONIAN AND TWO KINDS OF LAMB SHIFT

Now, we consider a time independent Schrödinger equation with whole space compromised of two subsystems as follows:

$$H_T |E\rangle_{AB} = E |E\rangle_{AB}, \quad (1)$$

where  $H_T$  is total (Hermitian) Hamiltonian with real energy eigenvalue  $E$ , and  $|E\rangle_{AB}$  represents the corresponding eigenvector of  $E$  on a given total system  $AB$ . For

convenience, each subspaces  $A$  and  $B$  denote a quantum system and an environment (or bath), respectively.

The first subspace is a discrete state of quantum system  $A$  and second one is a continuous scattering state of environment  $B$  such that projection operators  $\pi_A$ ,  $\pi_B$ , satisfies  $\pi_A + \pi_B = \mathbf{I}_T$  and  $\pi_A \pi_B = \pi_B \pi_A = 0$ . Here,  $\pi_A$  is a projection onto quantum system whereas  $\pi_B$  is a projection onto the environment. The operator  $\mathbf{I}_T$  is an identity operator defined on total space  $AB$ . With these projection operators, we can define block matrices such as  $h_A = \pi_A H_T \pi_A$ ,  $h_B = \pi_B H_T \pi_B$ ,  $V := V_{AB} = \pi_A H_T \pi_B$ , and  $V^\dagger := V_{BA} = \pi_B H_T \pi_A$ .

The total Hamiltonian in Eq. (1) can be represented by a block matrix form

$$H_T = h_A + h_B + V_{AB} + V_{BA}, \quad (2)$$

where  $h_A$  and  $h_B$  are the Hamiltonian of the system and environment, and  $V_{AB}$  and  $V_{BA}$  are interaction Hamiltonian between the system and the environment, respectively. The total wave function is also given by

$$|E\rangle_{AB} = \pi_A |E\rangle_{AB} + \pi_B |E\rangle_{AB} := |E\rangle_A + |E\rangle_B. \quad (3)$$

It is important to note that  $\pi_A |E\rangle_{AB} = |E\rangle_A$  and  $\pi_B |E\rangle_{AB} = |E\rangle_B$ . By using these relations, the Hamiltonian eigenvalue problem of Eq. (1) can be rewritten [17–20, 26] in the form of

$$\begin{aligned} (h_B - E) |E\rangle_B &= -V_{BA} |E\rangle_A \quad \text{and} \\ (h_A - E) |E\rangle_A &= -V_{AB} |E\rangle_B. \end{aligned} \quad (4)$$

Also note that the states restricted on  $A$  and  $B$  after the projections are given by [17]

$$\begin{aligned} |E\rangle_B &= |\mathcal{E}\rangle + G_B^\rightarrow V_{BA} |E\rangle_A \quad \text{and} \\ |E\rangle_A &= \frac{V_{AB}}{E - H_{\text{eff}}} |\mathcal{E}\rangle, \end{aligned} \quad (5)$$

where  $|\mathcal{E}\rangle$  is a eigenvector of  $h_B$  and  $G_B^\rightarrow$  is a outgoing Green function in the subspace  $B$ . The Eq. (5) means that the wave function localized in subsystem  $A$  can be obtained through the incoming wave  $|\mathcal{E}\rangle$  penetrating into the subsystem  $A$  via coupling term  $V_{AB}$  and propagating by effective Green function  $(E - H_{\text{eff}})^{-1}$ .

Then, by using the total Hamiltonian in Eq. (2), we can define the effective non-Hermitian Hamiltonian as

$$H_{\text{eff}} = h_A + V_{AB} G_B^\rightarrow V_{BA} \quad (6)$$

$$= h_A - \frac{1}{2} i V V^\dagger + P_v \int \frac{V V^\dagger}{E - \tilde{E}} d\tilde{E}, \quad (7)$$

where  $P_v$  means the (Cauchy) principal value depending on each decay channels.

This non-Hermitian Hamiltonian has generally complex eigenvalues under the Feshbach projection-operator formalism: (See Ref. [16] and the references therein.)

$$H_{\text{eff}} |\psi_k\rangle = \varepsilon_k |\psi_k\rangle \quad (8)$$

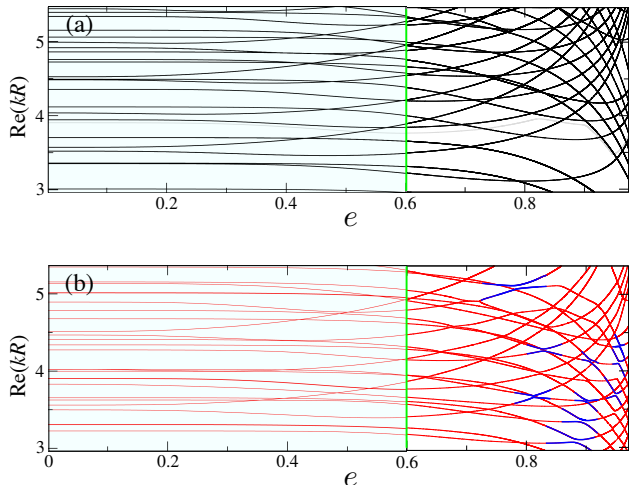


FIG. 2: The plot of  $\text{Re}(kR)$  versus the eccentricity  $e$  in ellipse. (a) The real value of  $kR$  in eigenvalue trajectories of the elliptic billiard depending on the eccentricity  $e$  from  $e = 0$  (circle) to  $e = 0.99$  (ellipse). There are not any avoided crossing in Fig. 2(a), since the elliptic billiard system is one of the integrable systems. (b) The real values of  $kR$  in eigenvalue trajectories of the elliptical microcavity for  $n = 3.3$  for refractive index of InGaAsP semiconductor microcavity depending on the eccentricity  $e$  from  $e = 0$  to  $e = 0.99$ . On the contrary to the elliptic billiard system, there are several avoided crossing marked by the blue lines beyond at  $e = 0.6$  in the open elliptic system. We set the green line in  $e=0.6$  to separate the region with avoided crossings and without avoided crossings.

and its eigenvalues of  $H_{\text{eff}}$  are given by (for each  $k$ )

$$\varepsilon_k = E_k - \frac{i}{2}\gamma_k. \quad (9)$$

Here,  $\varepsilon_k$  is an eigenvalue relating to  $E_k$  and  $\gamma_k$ , which represent the energy and decay width of the  $k$ -th eigenvector [17–20], respectively.

The Lamb shift, which is a small energy shift mentioned above, can be also obtained by the effective non-Hermitian Hamiltonian in Eq. (7) [16, 23]. That is,

$$\Delta H_{\text{Lamb}} := \text{Re}(H_{\text{eff}}) - h_A = P_v \int \frac{VV^\dagger}{E - \tilde{E}} d\tilde{E}. \quad (10)$$

If we consider the case of a two level system, then the Lamb shift can be obtained from a  $2 \times 2$ -matrix as a toy model:

$$\Delta H_{\text{Lamb}} = \begin{pmatrix} \omega_{11} & \omega_{12} \\ \omega_{21} & \omega_{22} \end{pmatrix}. \quad (11)$$

In general, the so-called *self-energy*  $S_e$  [13] due to the diagonal component  $\omega_{jj}$  is known as ‘‘Lamb shift’’ in atomic physics. On the other hand, the off-diagonal terms  $\omega_{jk}$  ( $\forall j, k = \{1, 2\}$ ) is known as ‘‘collective Lamb shift’’ by Rotter [23]. Therefore, the collective Lamb shift

leads to avoided resonance crossings (ARC) [32–34] obviously. So we can easily discriminate these two kinds of Lamb shift as shown in Fig. 2. There are two kinds of real values of  $kR$  in the eigenvalue trajectories depending on the eccentricity  $e$  from  $e = 0$  (circle) to  $e = 0.99$  (ellipse). The black solid lines are the eigenvalue trajectories of  $\text{Re}(kR)$  of the elliptic billiard, and the red solid lines are those of the elliptic microcavity interacting with its environment (open quantum system). According to the random matrix theory [35], the integrable system, which has  $N$  quantum number in  $N$  degree of freedom, is followed by Poisson distribution resulting without avoided crossing. This fact is well-conformed by Fig. 2(a). There are always level crossings even at large eccentricity, i.e.,  $e = 0.99$ .

On the contrary, we can check that there are several avoided crossing marked by blue lines in the elliptic microcavity beyond  $e = 0.6$ . These resonance repulsion must be originated from off-diagonal term  $\omega_{jk}$ , i.e., the collective Lamb shift. As a result, we can distinguish between self-energy region and collective Lamb shift region by checking the existence of avoided crossings. In order to consider only self-energy region, we set a green vertical line at  $e = 0.6$ . We remark that a study on collective Lamb shift will be published soon.

#### IV. GLOBAL TRANSITION OF SELF-ENERGY AND DECAY CHANNEL

Lamb shift was first observed at hydrogen atom [12], and then it has been studied at cavity QED [15] and photonic crystals [14] and so on. In this section, we investigate the geometrical boundary dependence of Lamb shift (self-energy) through global transitions depending on  $e$ . There are real values  $kR$  in eigenvalue trajectories of single layer whispering gallery modes (WGMs) of  $\ell = 1$  and  $m = (3, 4, 5, 6, 7)$  for orange lines depending on eccentricity  $e$  in both elliptic billiard and microcavity, respectively in Fig. 3(a). The solid lines are eigenvalue trajectories of an elliptic billiard whereas the dotted lines are those of the elliptic microcavity. We can easily check that the relative difference of two eigenvalue trajectories are almost unchanged even at the eccentricity  $e = 0.6$ . In Fig. 3(b), there are the real  $kR$  in eigenvalue trajectories of  $(m = 3, \ell = 2, 3, 4, 5, 6)$ , and  $(m = 4, \ell = 2, 3, 4, 5, 6)$ ,  $(m = 5, \ell = 2, 3, 4, 5, 6)$ , respectively, and depending on the eccentricity  $e$  in both elliptic billiard and microcavity. The black lines are for  $m = 3$  and the reds are for  $m = 4$ , blues are for  $m = 5$ , respectively. On the contrary to the single layer WGMs, the relative differences between two kinds of eigenvalue trajectories are drastically changed near at  $e = 0.4$ . As we defined self-energy in Sec. III, these relative differences of two kinds of eigenvalue trajectories are the self-energy ( $S_e$ ).

These patterns of the self-energy transition depending on the eccentricity  $e$  are clearly shown in Fig. 4 below. We here notice that there are primarily three types of the

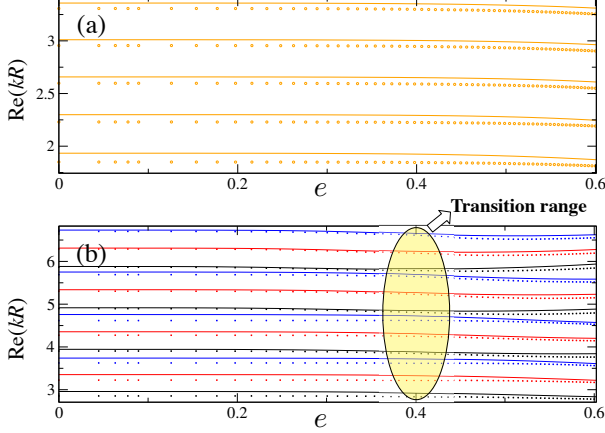


FIG. 3: (a) The real  $kR$  in eigenvalue trajectories of single layer whispering gallery mode of  $\ell = 1$  and  $m = (3, 4, 5, 6, 7)$  depending on the eccentricity  $e$  in both elliptic billiard and microcavity. The solid lines are eigenvalues of the elliptic billiard, and dotted lines are those of elliptic microcavity. The difference between two eigenvalues are almost unchanged even at  $e = 0.6$ . (b) The real  $kR$  in eigenvalue trajectories of ( $m = 3, \ell = 2, 3, 4, 5, 6$ ), and ( $m = 4, \ell = 2, 3, 4, 5, 6$ ), ( $m = 5, \ell = 2, 3, 4, 5, 6$ ) respectively depending on the eccentricity  $e$  in both elliptic billiard and microcavity. On the contrary to the single layer whispering gallery mode, the difference between two eigenvalues are drastically changed at  $e = 0.4$ .

self-energy transitions represented by increasing group ( $\triangleright$ ), decreasing group ( $\triangleright$ ), and unchanging group ( $\triangleright$ ), respectively. In the case of increasing and decreasing groups, the figures also show that the transition rate of the self-energy is very small until  $e = 0.3$ , but rapidly increasing beyond the eccentricity  $e = 0.3$ . Furthermore, we can also observe that the self-energy of the increasing group and the decreasing group meet at  $e \simeq 0.5$ , which means the crossings of the self-energy take place near at  $e = 0.5$ . That is,

$$\Delta S_e := |\omega_{jj} - \omega_{kk}| = 0. \quad (12)$$

First, we study how the three types of transitions can be classified into. In order to do that, we get the Husimi probability distributions superimposed by PSOS all of them at  $e = 0.6$ . As a result, these distributions are classified into three types of motions according to whispering gallery (WG) modes, stable-bouncing (SB) ball modes and unstable-bouncing (UB) modes, respectively. We plot one of the Husimi probability distributions in each group. The Fig. 5(a) is one of the unchanging group, i.e., ( $\ell = 1, m = 7$ ). This resonance is well-localized on the intact invariant curves. The Fig. 5(b) is one of the increasing group, i.e., ( $\ell = 5, m = 5$ ). This resonance mode is well-localized on stable-bouncing ball region. The Fig. 5(c) is one of the decreasing group, i.e., ( $\ell = 3, m = 5$ ). This resonance mode is also well-

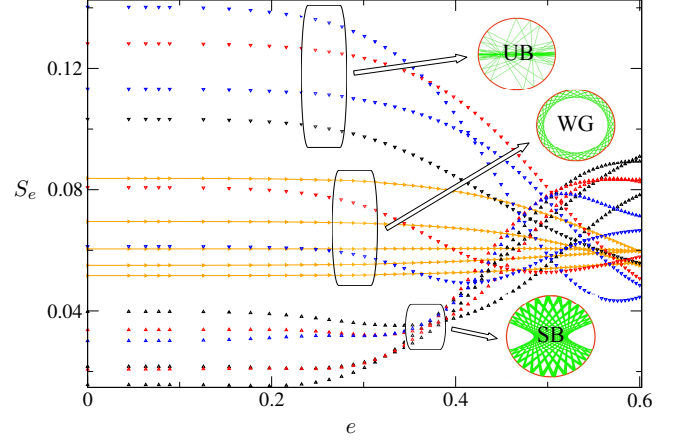


FIG. 4: The transitions of self-energy  $S_e$  of Fig. 3 depending on the eccentricity  $e$ . There are primary three-type of the self-energy transitions; whispering gallery (WG represented by  $\triangleright$ ), stable-bouncing (SB represented by  $\diamond$ ), and unstable-bouncing (UB represented by  $\nabla$ ) modes, respectively. The SBs exhibit increasing pattern of self-energy, UBs exhibit decreasing of self-energy, and WGs exhibit almost unchanging of self-energy, respectively. In the case of bouncing ball type modes, the figures also show that the transition rate of the self-energy is getting rapidly increasing beyond  $e = 0.3$ , and the crossing of the self-energy takes place near at  $e = 0.5$ .

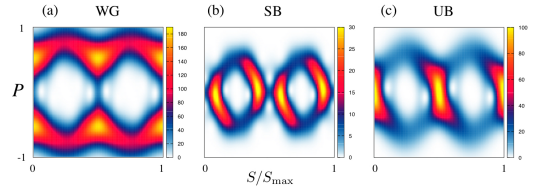


FIG. 5: The Husimi probability distributions superimposed on PSOS. (a) One of the unchanging self-energy group, i.e.,  $\ell = 1, m = 7$ . This whispering gallery mode is well-localized on the intact invariant curves. (b) One of the increasing self-energy group, i.e.,  $\ell = 5, m = 5$ . This resonance mode is well-localized on stable-bouncing ball region. (c) One of the decreasing self-energy group, i.e.,  $\ell = 3, m = 5$ . This resonance mode is well-localized on the unstable-bouncing ball region.

localized on the unstable-bouncing ball region. Even though we do not exhibit all of the Husimi probability distributions, we can conclude that without loss of generality, unchanging groups are corresponding to the whispering gallery modes group and the increasing groups are corresponding to the stable-bouncing ball modes group, the decreasing groups are corresponding to the unstable-bouncing ball modes group, respectively.

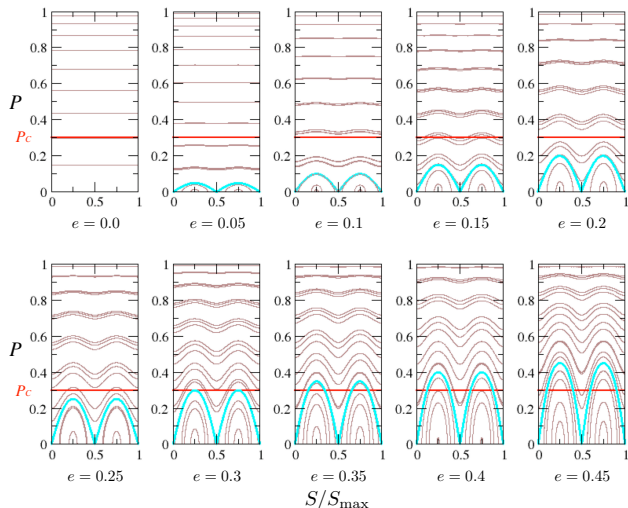


FIG. 6: The Poincaré surface of sections with separatrices and the critical lines at  $e = 0.0$ ,  $e = 0.05$ ,  $e = 0.1$ ,  $e = 0.15$ ,  $e = 0.2$ ,  $e = 0.25$ ,  $e = 0.3$ ,  $e = 0.35$ ,  $e = 0.4$ , and  $e = 0.45$ , respectively. The critical lines whose colors are red are placed near at  $P_c = 0.3$ . The stable island structure is becoming larger as  $e$  increases. Thus the separatrix whose colors are cyan are going up as  $e$  increases. The separatrix touch the critical line near at  $e \simeq 0.3$  and keep soaring into the critical line beyond  $e \simeq 0.3$ .

Second, we investigate why the transition rate of bouncing ball mode groups can be abruptly increased near at  $e = 0.3$ . It can be explained by PSOS with critical lines and separatrices depending on the eccentricity  $e$ . In Fig. 6, there are Poincaré surface of sections of the elliptic billiard with separatrices and critical lines at  $e = 0.0$ ,  $e = 0.05$ ,  $e = 0.1$ ,  $e = 0.15$ ,  $e = 0.2$ ,  $e = 0.25$ ,  $e = 0.3$ ,  $e = 0.35$ ,  $e = 0.4$ , and  $e = 0.45$ , respectively. The critical lines whose colors are red are placed near at  $P_c = 0.3$ . In classical regime, i.e., ray dynamics, the light can not leak out below this critical line. These separatrices whose colors are cyan are border lines of between the whispering gallery motions and bouncing ball motions. We also notice that the stable island structure is becoming larger as  $e$  increases. Thus it means that the separatrices are also going up as  $e$  increases. These separatrices still remain below critical line until  $e = 0.3$  but they touch the critical line near  $e = 0.3$  and keep soaring into critical line beyond  $e = 0.3$ . This fact implies that the decay channels of the bouncing ball-type modes undergo severe transitions during the separatrices crossing the critical line. Because the self-energy is defined for each decay channel, these transition of decay channel explain the transitions of self-energy. In the case of whispering gallery motions, since the invariant curves in PSOS are nearly unchanged comparing to bouncing ball type motions, their global transitions are also nearly unchanged comparing to them.

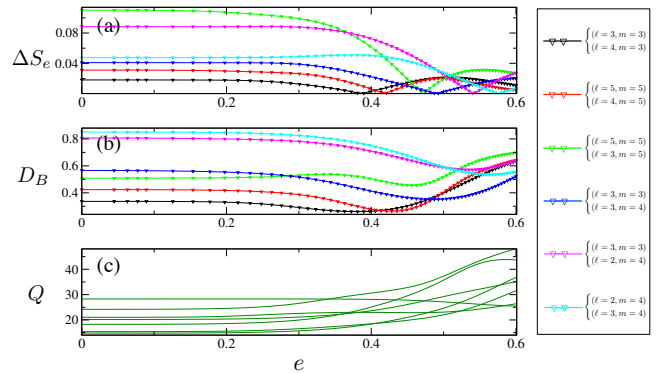


FIG. 7: (a) Several selected relative differences of the self-energy ( $\Delta S_e$ ) depending on  $e$ . The black curve is one for  $\Delta S_e$  between originated from  $\ell = 3, m = 3$  and  $\ell = 4, m = 3$ . The red curve is one for  $\Delta S_e$  between originated from  $\ell = 5, m = 5$  and  $\ell = 4, m = 5$  and the green, blue, magenta, cyan curves are ones for  $\Delta S_e$  between originated from  $[(\ell = 5, m = 5), (\ell = 3, m = 5)]$ ,  $[(\ell = 3, m = 4), (\ell = 3, m = 3)]$ ,  $[(\ell = 3, m = 3), (\ell = 2, m = 4)]$ , and  $[(\ell = 2, m = 4), (\ell = 3, m = 4)]$ , respectively. (b) The Bhattacharyya distance ( $D_B$ ) of Husimi probability distributions below the critical line associated with same pair of  $\Delta S_e$ . This relation directly measures the similarity of decay channels. (c) The quality factors  $Q$  associated with same pair of  $\Delta S_e$ .

## V. SELF-ENERGY VERSUS HUSIMI DISTRIBUTION FUNCTION

The crossing of self energy,  $\Delta S_e = 0$  for bouncing ball group, takes place near at  $e = 0.5$ . Our conjecture is that, since the self-energy is defined for each decay channel, the crossings of the self-energy may take place when a pair of compared resonances shares larger common decay channels.

In order to conform that, we select five pairs of relative differences of self-energy ( $\Delta S_e = |\omega_{jj} - \omega_{kk}|$ ) depending on  $e$ . These curves are shown in Fig. 7(a). The black curve is one for  $\Delta S_e$  between originated from  $[(\ell = 3, m = 3), (\ell = 4, m = 3)]$ . The red curve is one for  $\Delta S_e$  between originated from  $[(\ell = 5, m = 5), (\ell = 4, m = 5)]$  and the green, blue, magenta, and cyan curves are ones for  $\Delta S$  between originated from  $[(\ell = 5, m = 5), (\ell = 3, m = 5)]$ ,  $[(\ell = 3, m = 3), (\ell = 3, m = 4)]$ ,  $[(\ell = 3, m = 3), (\ell = 2, m = 4)]$ , and  $[(\ell = 2, m = 4), (\ell = 3, m = 4)]$ , respectively. Even though all these values are almost unchanged until at  $e = 0.3$ , beyond this point, they decrease and have zero values and then increase again. The zero point of  $\Delta S_e$  ( $\Delta S_e = 0$ ) for black is near at  $e = 0.38$  and for red is near at  $e = 0.42$ , for green is  $e = 0.47$ , for blue is  $e = 0.49$ , for magenta is  $e = 0.54$  and for cyan is  $e = 0.57$ , respectively.

Since the decay channels are controlled by Husimi distributions below the critical line [27–29], we measure

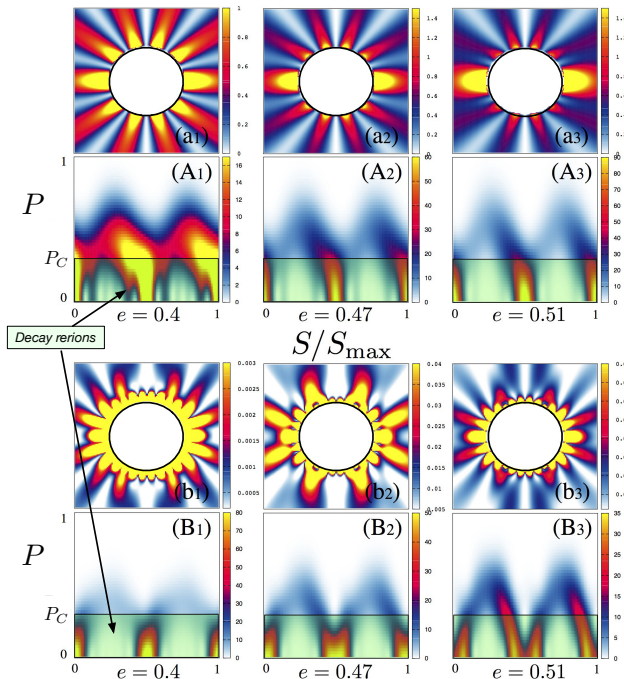


FIG. 8: The intensity plots of resonance tails and Husimi probability distributions for  $(\ell = 3, m = 5)$  in the indexes  $(a_j)$  and  $(A_j)$ , and  $(\ell = 5, m = 5)$  in  $(b_j)$  and  $(B_j)$  at  $e = 0.4$ ,  $e = 0.47$ , and  $e = 0.51$ , respectively. The Husimi probability distributions are very similar at  $e = 0.47$ . This fact conforms that the Bhattacharyya distance  $D_B$  has lowest value at  $e = 0.47$

the similarity of Husimi distributions below the critical line to define the degree of sharing common decay channel. In this reason, we employ the Bhattacharyya distance [30, 31] for investigating the similarity of the decay channels (Husimi distributions below the critical line). The Bhattacharyya distance measures the similarity of different two probabilities. For probability distribution  $p(x)$  and  $q(x)$ , it is defined by

$$D_B(p(x), q(x)) = -\ln [\kappa_B(p(x), q(x))], \quad (13)$$

where the factor  $\kappa_B$  (namely, Bhattacharyya coefficient) is given by

$$\kappa_B(p(x), q(x)) = \int \sqrt{p(x)q(x)} dx. \quad (14)$$

Note that the Bhattacharyya coefficient measures the amount of overlap between two statistical populations, i.e., classical fidelity [31]

In Fig. 7(b), there are Bhattacharyya distance  $D_B$  obtained from the decay channels associated with same pair of  $\Delta S_e$  of Fig. 7(a). The global transition patterns are very similar to those of  $\Delta S_e$ . That is, the global transition patterns of  $\Delta S_e$  and  $D_B$  show sharp parabola and

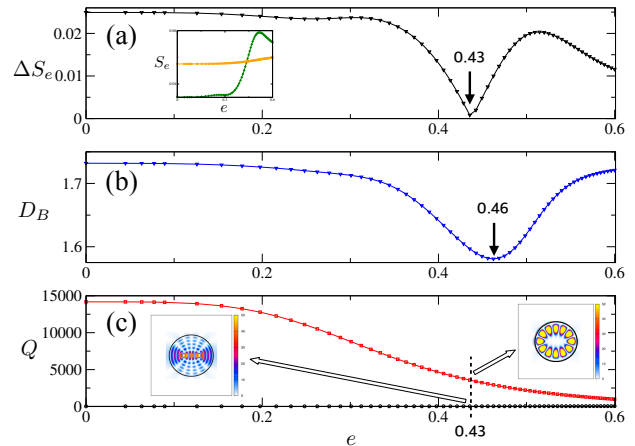


FIG. 9: (a) Relative differences of self-energy ( $\Delta S_e$ ) between single layer WGMs ( $\ell = 1$  and  $m = 6$ ), and stable-bouncing ball-type mode ( $\ell = 5$  and  $m = 5$ ) depending on  $e$ . Its minimum values are lying on at  $e = 0.43$ . (b) The Bhattacharyya distance  $D_B$  of Husimi distribution below the critical line associated with same pair of  $\Delta S_e$ . Its minimum values are at  $e = 0.46$ . The absolute magnitude of  $D_B$  is much larger than those of Fig. 7(b). (c) The quality factors ( $Q$ ) associated with same pair of  $\Delta S_e$ . These two quality factors (red and black lines with dots) do not have similar order of magnitude.

smooth parabola at same region, respectively. Note that each extremal points of curves  $\Delta S_e$  and  $D_B$  is almost coincident at each  $e = 0.38$ ,  $e = 0.42$ ,  $e = 0.47$ ,  $e = 0.49$ ,  $e = 0.54$ , and  $e = 0.57$ , respectively. We also notice in Fig. 7(c) that the quality factors of resonances involved in Fig. 7(a) show similar degree of magnitude.

There are intensity plots of eigenfunctions and Husimi probability distributions for  $(\ell = 5, m = 3)$  with indexes  $(a_j)$  and  $(A_j)$  in Fig. 8, and  $(\ell = 5, m = 5)$  with  $(b_j)$  and  $(B_j)$  of Fig. 8 at  $e = 0.4$ ,  $e = 0.47$ , and  $e = 0.51$ , respectively. The plots  $(a_j)$  and  $(b_j)$  are resonance tales determined by Husimi probability distributions below critical lines represented by green shadow regions. These resonance tales play the role of decay channels [16, 28]. We can easily notice that the green shadow regions are very similar at  $e = 0.47$ . This fact conforms that the Bhattacharyya distance  $D_B$  has lowest value at  $e = 0.47$ .

We also investigate the relation of  $\Delta S_e$  and  $D_B$  between single layer WGM ( $\ell = 1$  and  $m = 6$ ) and stable-bouncing ball-type mode ( $\ell = 5$  and  $m = 5$ ) depending on the eccentricity  $e$ . Their extremal positions are lying on at  $e \simeq 0.43$  and  $e \simeq 0.46$ , respectively. These are shown in Fig. 9(a) and Fig. 9(b). For the inset (a) of Fig. 9, the orange curve is  $S_e$  for  $\ell = 1, m = 6$  and the green one is  $S_e$  for  $\ell = 5, m = 5$ , respectively. The quality factors  $Q$  of associated with same pair of Fig. 9(a) are shown in Fig. 9(c) and these two quality factors do not have similar order of magnitude also. We can figure out that

even though the quality factors of comparing resonances are rather different from each other, if they share common decay channel in *narrow* parameter range, i.e., the parabola is manifested in the Bhattacharyya distance  $D_B$  curve, the global transition of  $\Delta S_e$  is strongly controlled by  $D_B$ . According to the result of Fig. 7 and Fig. 9, we conjecture that if their quality factors have more similar degree of magnitude, the vertices of  $S_e$  and  $D_B$  will be more coincident. Note that the absolute magnitude of  $D_B$  of between WGM and stable-bouncing ball mode is much larger than those of between bouncing ball type modes in Fig. 7(a). This is a natural result, because the similarity between two bouncing ball type modes is much larger than that of between WGM and stable-bouncing ball modes.

## VI. CONCLUSION

We have studied the geometrical boundary dependence of Lamb shift (self-energy) through global transitions in elliptic microcavity. We select self-energy region by choosing without an avoided resonance crossing (ARC) region. We confirm that these three types as a global transition are corresponding to the whispering gallery modes, stable-bouncing ball modes, and unstable-bouncing ball modes, respectively by Husimi distributions superimposed by classical Poincaré surface of sections. These facts directly indicate that the decay channel of an elliptic microcavity also can be classified into these three types of modes, because the self-energy is defined for each decay channel. The rate of global transition of self-energy is abruptly increased beyond  $e \simeq 0.3$ , since

the separatrix touch the critical line near at  $e = 0.3$ , which means that the decay channels of bouncing ball motions are abruptly changed around this region.

We also have investigated the crossings of self-energy, i.e.,  $\Delta S_e = 0$ . These self-energy crossings take place in the region where the resonances share much larger common decay channels in *narrow* parameter range. We confirm this fact by the Bhattacharyya distance  $D_B$ . The curves of relative differences of the self-energy ( $\Delta S_e$ ) and the Bhattacharyya distance ( $D_B$ ) show very similar patterns, and the extremal points of the parabola of these two curves are almost coincident. The extremal positions of two curves  $\Delta S_e$  and  $D_B$  are getting closer as the difference between the quality factor of two modes gets smaller. This facts imply that  $\Delta S_e$  more depends on  $D_B$  as the difference of the interaction of system-environment of two modes gets smaller. Our results give not only the understanding of Lamb shift in microcavity but also the implications of openness effect theoretically and systematically.

## VII. ACKNOWLEDGEMENT

This work was partly supported by the IT R&D program of MOTIE/KEIT [10043464]. We thank Korea Institute for Advanced Study for providing computing resources (KIAS Center for Advanced Computation Linux Cluster) for this work. K.J. acknowledges financial support by the National Research Foundation of Korea (NRF) Grant funded by the Korea government (MSIP) (Grant No. 2010-0018295) and the Associate Member Program funded by the Korea Institute for Advanced Study.

- 
- [1] S. Shinohara, T. Harayama, and T. Fukushima, *Opt. Lett.* **36**, 1023 (2011).
  - [2] N. B. Rex, H. E. Tureci, H. G. L. Schwefel, R. K. Chang, and A. D. Stone, *Phys. Rev. Lett.* **88**, 094102 (2002).
  - [3] H. Schomerus and M. Hentschel, *Phys. Rev. Lett.* **96**, 243903 (2006).
  - [4] J. Unterhinninghofen, J. Wiersig, and M. Hentschel, *Phys. Rev. E* **78**, 016201 (2008).
  - [5] S.-Y. Lee, S. Rim, J.-W. Ryu, T.-Y. Kwon, M. Choi, and C.-M. Kim, *Phys. Rev. Lett.* **93**, 164102 (2004).
  - [6] S.-B. Lee, J. Yang, S. Moon, S.-Y. Lee, J.-B. Shim, S. W. Kim, J.-H. Lee, and K. An, *Phys. Rev. Lett.* **103**, 134101 (2009).
  - [7] W. D. Heiss, *J. Phys. A: Math. Gen.* **37**, 2455 (2004).
  - [8] M. Müller and I. Rotter, *J. Phys. A: Math. Gen.* **41**, 244018 (2008).
  - [9] D. L. Kaufman, I. Kosztin, and K. Schulten, *Am. J. Phys.* **67**, 133 (1999).
  - [10] H.-J. Stöckmann, *Quantum Chaos: An Introduction* (Cambridge University Press, London, 1999).
  - [11] H. Waalkens, J. Wiersig, and H. R. Dullin, *Ann. Phys.* **260**, 50 (1997).
  - [12] W. E. Lamb Jr., and R. C. Retherford, *Phys. Rev.* **72**, 241 (1947).
  - [13] M. O. Scully and A. A. Svidzinsky, *Science* **328**, 1239 (2010).
  - [14] X.-H. Wang, Y. S. Kivshar, and B.-Y. Gu, *Phys. Rev. Lett.* **93**, 073901 (2004).
  - [15] B. H. Nguyen, *Adv. Nat. Sci.: Nanosci. Nanotechnol.* **1**, 035008 (2010).
  - [16] K.-W. Park, J. Kim, and K. Jeong, *Opt. Commun.* **368**, 190 (2016).
  - [17] I. Rotter, *J. Phys. A: Math. Theor.* **42**, 153001 (2009).
  - [18] F.-M. Dittes, *Phys. Rep.* **339**, 215 (2000).
  - [19] G. L. Celardo and L. Kaplan, *Phys. Rev. B* **79**, 155108 (2009).
  - [20] J. Wiersig, S. W. Kim, and M. Hentschel, *Phys. Rev. A* **78**, 053809 (2008).
  - [21] R. Röhlsberger, H.-C. Wille, K. Schlage, and B. Sahoo, *Nature* **482**, 199 (2012).
  - [22] R. Röhlsberger, K. Schlage, B. Sahoo, S. Couet, and R. Ruffer, *Science* **328**, 1248 (2010).
  - [23] I. Rotter, *Fortschr. Phys.* **61**, 178 (2013).
  - [24] M. Tabor, *Chaos and integrability in nonlinear dynamics: an introduction* (Wiley, 1989).
  - [25] J. U. Nöckel, Yale University (Ph.D. Thesis), 1997.

- [26] N. Moiseyev, *Non-Hermitian Quantum Mechanics* (Cambridge University Press, London, 2011).
- [27] Q. H. Song, L. Ge, A. D. Stone, H. Cao, J. Wiersig, J.-B. Shim, J. Unterhinninghofen, W. Fang, and G. S. Solomon, Phys. Rev. Lett. **105**, 103902 (2010).
- [28] Q. Song, Z. Gu, S. Liu, and S. Xiao, Sci. Rep. **4**, 4858 (2014).
- [29] J. Wiersig and M. Hentschel, Phys. Rev. Lett. **100**, 033901 (2008).
- [30] A. Bhattacharyya, Bull. Cal. Math. Soc. **35**, 99 (1943).
- [31] D. Markham, J. A. Mischak, Z. Puchała, and K. Życzkowski, Phys. Rev. A **77**, 042111 (2008).
- [32] J.-W. Ryu, S.-Y. Lee, and S. W. Kim, Phys. Rev. A **79**, 053858 (2009).
- [33] J. Wiersig, Phys. Rev. Lett. **97**, 253901 (2006).
- [34] Q. Song, L. Ge, J. Wiersig, and H. Cao, Phys. Rev. A **88**, 023834 (2013).
- [35] F. Haake, *Quantum Signatures of Chaos* (Springer, Berlin, 2010).